Design of a vibration energy harvester with two close resonant frequencies

David Gibus, Adrien Morel, Ludovic Charleux, Aya Benhemou, Adrien Badel, Pierre Gasnier

Design of a vibration energy harvester with two close resonant frequencies

Abstract—**We present the design of a piezoelectric cantilever with a L-shaped proof mass and multiples electrodes allowing vibration energy harvesting at two close frequencies. Indeed, the resonant frequencies of the proposed harvester are 35.3 Hz and 53.2 Hz for the first and second bending modes, respectively. Based on a study of the strain distribution with an analytical model, we provide design guidelines for the electrodes' configuration to maximize the electromechanical coupling coefficients k^2 of a PZT-based harvester. When the electrodes are judiciously connected, the coefficient k^2 reaches 9.3 % for the first mode and 8.1 % for the second mode, allowing 3 Hz (8.4 %) and 3.5 Hz (6.5 %) frequency bandwidths with resistive frequency tuning respectively.**

I. INTRODUCTION

Piezoelectric vibration energy harvesters are a promising technology that has been widely investigated during the last two decades to power wireless sensor nodes. The commonly designed linear piezoelectric resonators can harvest energy only on a limited frequency range around their resonant frequencies. Such narrow frequency bandwidth constitutes a major issue of vibration energy harvesters.

As a response, Moon *et al.* proposed in 2018 to design a tunable proof mass on a piezoelectric cantilever in order to minimize the frequency difference between the two first bending modes of their harvester [1]. Such a system represents a promising solution to harvest energy from vibration source that have two close frequencies with high energy density. Indeed, the second resonant frequency is at least 6.27 times greater than the first resonant frequency for cantilever with conventional proof mass [2]. In order to minimize this frequency gap, Erturk *et al.* already proposed in 2009 to add a secondary beam orthogonally to the primary cantilever [2]. The proposed prototype exhibits a frequency ratio of almost 2. While this harvester is suitable for drone applications, it was not suitable for energy harvesting in a confined space because the height of the system is significant. Meanwhile, a L-shape proof mass has been shown relevant on a piezoelectric cantilever in order to maximize the power density at the first resonant frequency by Li *et al.* in 2010 [3]. However, the authors did not provide any insights concerning the second bending mode. It is a similar configuration (L-shape proof mass) that Moon *et al.* considered in order to bring the two first resonant frequencies closer [1]. Although their results were promising since the two resonant frequencies were experimentally nearly equal, charge cancellation on the piezoelectric electrodes was not considered in their work. Indeed, Erturk *et al.* showed that the second bending mode induces a charge cancellation in cantilever with conventional proof mass due to sign changes in the strain distribution in the beam [4]. Such charge cancellation can induce a drastic decrease of the global electromechanical coupling coefficient k^2 of the harvester if the electrodes are injudiciously configured. As k^2 is of a prior importance to maximize the harvested power and the frequency bandwidth in case of electrical resonant frequency tuning [5], the strain distribution and the electrode configuration should not be neglected in the

design of vibration energy harvesters. While the use of L-shape proof mass affects the strain distribution as well as the resonant frequencies, no analysis of the strain distribution on the two first bending mode was performed in the literature.

The present work studies the strain distribution and the electrode configuration of piezoelectric cantilevers with L-shape proof mass and with conventional proof mass in the purpose of maximizing their electromechanical coupling coefficient. Our study relies on modelling, FEM simulations and experiments. The model is presented in the next section. The third section shows how to use the model on a case study and the fourth section is dedicated to the prototype presentation and experimental validation.

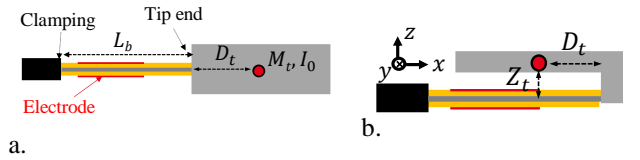## II. DEVICE AND MODELLING

A. Device presentation

Fig. 1: a. Cantilever with conventional proof mass ($D_t > 0$) b. cantilever with L-shaped proof mass ($D_t < 0$)

The studied harvester is a piezoelectric bimorph with a proof mass (Fig. 1). The piezoelectric layers and the substrate have the same length (L_b) and the same width (B) as the beam. The piezoelectric layers are partially covered by electrodes. The proof mass considered as infinitely rigid is modeled by an equivalent point mass described by a mass M_t and a rotational inertia I_O placed at a coordinate D_t from the free end of the beam along the x-axis. If the proof mass is asymmetric according the neutral axis, the projection on the neutral axis of the rotary inertia, noted I_t, is calculated by considering the distance Z_t with the Huygens theorem:

$$I_t = I_0 + M_t Z_t^2 \tag{1}$$

D_t can be either positive for conventional proof mass (Fig. 1.a.), either negative for L-shaped proof mass (Fig. 1.b.). The electrodes size and position (Fig. 1) have yet to be determined and will be discussed in the next sections.

B. Modelling

Assuming the Euler-Bernoulli assumption and neglecting the beam mass compared to the proof mass, we use the 2 degree of freedom analytical model from [5]. The longitudinal strain S_1 in the beam is therefore expressed by the equation (2) where $\phi_i(x)$ is the ith bending mode shape (with $i \in \{1; 2\}$), $r_i(t)$ is the generalized coordinate of the ith mode corresponding to the relative transverse displacement at the tip end ($x = L_b$). z is the position from the neutral axis of the beam.

From equation (2), $\phi_i''(x)$ represents the longitudinal strain distribution in the beam for the ith mode. According to the model, it is an affine function that depends on two coefficients a_i and b_i, as expressed in (3).

$$S_1 = \sum_{i=1}^{2} -z\phi_i''(x)r_i(t) \qquad (2)$$

$$\phi_i''(x) = b_i + a_i\left(1 - \frac{x}{L_b}\right) \qquad (3)$$

a_1, b_1, a_2 and b_2 are expressed in (4), (5), (6) and (7) respectively with Γ a coefficient expressed in (8). The rotary inertia to mass ratio J_t expressed as $J_t = \frac{I_t}{M_t}$ depends on the proof mass shape.

$$a_1 = \frac{6\left(6J_t - 2\sqrt{\Gamma} + 6D_T^2 + L_b^2 + 6D_T L_b\right)}{L_b^3\left(3J_t - \sqrt{\Gamma} + 3D_T^2 - L_b^2\right)} \qquad (4)$$

$$b_1 = -\frac{6\left(3J_t - \sqrt{\Gamma} + 3D_T^2 + L_b^2 + 4D_T L_b\right)}{L_b^2\left(3J_t - \sqrt{\Gamma} + 3D_T^2 - L_b^2\right)} \qquad (5)$$

$$a_2 = \frac{6\left(6J_t + 2\sqrt{\Gamma} + 6D_T^2 + L_b^2 + 6D_T L_b\right)}{L_b^3\left(3J_t + \sqrt{\Gamma} + 3D_T^2 - L_b^2\right)} \qquad (6)$$

$$b_2 = -\frac{6\left(3J_t + \sqrt{\Gamma} + 3D_T^2 + L_b^2 + 4D_T L_b\right)}{L_b^2\left(3J_t + \sqrt{\Gamma} + 3D_T^2 - L_b^2\right)} \qquad (7)$$

$$\Gamma = 9D_T^4 + 18D_T^3 L_b + 15D_T^2 L_b^2 + 18D_T^2 J_t + 6D_T L_b^3 \\ + 18D_T L_b J_t + L_b^4 + 3L_b^2 J_t + 9J_t^2 \qquad (8)$$

A representation of a_i and b_i is provided in Fig. 2 for a cantilever beam with a regular proof mass. Equations (2), (3) and Fig. 2 show that the longitudinal distribution of strain only depends on the coefficients a_i and b_i.
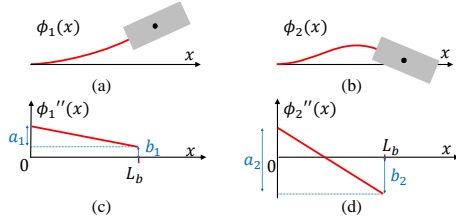

Fig. 2: Mode shapes and strain distributions for conventional proof mass.

Although Fig. 2 shows a conventional proof mass, the model is valid for any form of proof mass, including L-shaped one in Fig. 1.b., since the proof mass is rigid relative to the beam and more than twice as heavy as it.

Considering the model, the alternative electromechanical coupling coefficient k_{ei}^2 (with $k_e^2 = k^2/(1-k^2)$) of the two first bending modes i is expressed by equation (9) when the piezoelectric patches are fully covered with electrodes. k_{e31}^2 is called the expedient coupling coefficient of the piezoelectric material according to the 31-mode ($k_{e31}^2 = k_{31}^2/(1-k_{31}^2)$).

$$k_{ei}^2 = k_{e31}^2 \mathcal{R}_{Li} \mathcal{R}_T \qquad (9)$$

$\mathcal{R}_{Li}$ and $\mathcal{R}_T$ are length and thickness factors respectively. $\mathcal{R}_T$ is related to the stress distribution in the thickness of the beam and is expressed in (10) . Y_s is the Young modulus of the substrate, c_{11} is the linear elastic coefficient of the piezoelectric material according to the plane stress assumption. $\mathcal{R}_T$ does not depend on the bending mode.

$$\mathcal{R}_T = \frac{\left(\frac{h_p}{h_s}\right)^3 + 2\left(\frac{h_p}{h_s}\right)^2 + \left(\frac{h_p}{h_s}\right)}{\frac{1}{6}\left(\frac{Y_s}{c_{11}}\right) + \frac{4 + k_{e31}^2}{3}\left(\frac{h_p}{h_s}\right)^3 + 2\left(\frac{h_p}{h_s}\right)^2 + \left(\frac{h_p}{h_s}\right)} \qquad (10)$$

As expressed in equation (11), $\mathcal{R}_{Li}$ only depends on the ratio b_i and a_i.

$$\mathcal{R}_{Li} = \frac{\left(\frac{b_i}{a_i}\right)^2 + \left(\frac{b_i}{a_i}\right) + \frac{1}{4}}{\left(\frac{b_i}{a_i}\right)^2 + \left(\frac{b_i}{a_i}\right) + \frac{1}{3}} \qquad (11)$$

In order to maximize the global coupling coefficient k^2 of a piezoelectric cantilever, the electrodes must be placed on the piezoelectric patches in the region where the elastic energy is maximized and uniformly distributed [6]. In other words, the electrodes should be located along the length where the strain distribution $\phi''(x)$ is maximized and with limited variation. For this reason, the coefficients a_i and b_i need to be evaluated with respect to the proof mass configuration. As the strain distribution and the resonant frequencies depend on the position of the proof mass (i.e. the value of D_t), the influence of D_t on the resonant frequencies, a_i and b_i will be further discussed in the next section.

III. ANALYSIS

We consider the case of study of a cantilever made of steel and PZT NCE51 from Noliac company. The geometric parameters are given in Table 1. Fig. 3 represents the short-circuit (i.e. patches fully covered with electrodes connected to the ground) resonant frequencies calculated with expressions from [5] for the two first bending modes as a function of D_t.

Table 1: Geometrical parameters considered for the study

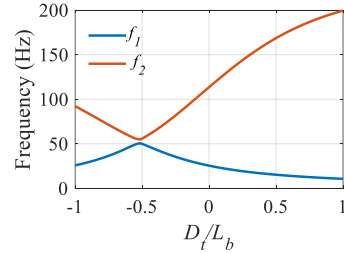|	
Beam length L_b	60 mm
Substrate thickness h_s	0.4 mm
Patches thickness h_p	0.3 mm
Beam and proof mass width B	5 mm
Mass of the proof mass M_t	0.06 kg
Rotary inertia	2.5×10^{-5} kg.m^2

Fig. 3: Short-circuit resonant frequencies from the model

The two resonant frequencies get closer when D_t is around $-0.5L_b$ (i.e., the center of gravity of the proof mass is around the middle of the beam). The exact value of D_t/L_b for which the two resonant frequencies are closest actually depends on many parameters such as I_t and M_t, as discussed in [1], but, according to calculations made with many parameter sets, this value is never very far from the range [-0.6:-0.4].

According to equations (4) to (8), the longitudinal distribution of strain only depends on D_t, L_b and J_t. Fig. 4 shows the strain distribution $\phi''(x)$ deduced from equations (4) to (8) and (3) and normalized by its maximal value ($\phi''(x)/\max[\phi''(x)]$) for 3 values of D_t and the two first bending modes.

Fig. 4 reveals that the longitudinal distribution of strain depends on the value of D_t. Considering the design of

piezoelectric cantilevers, the piezoelectric patches have to be placed at the location where $\phi''(x)$ is maximal.

Fig. 4: Strain distribution for a. $D_t = 0$, b. $D_t = -0.35L_b$ and c. $D_t = -L_b$
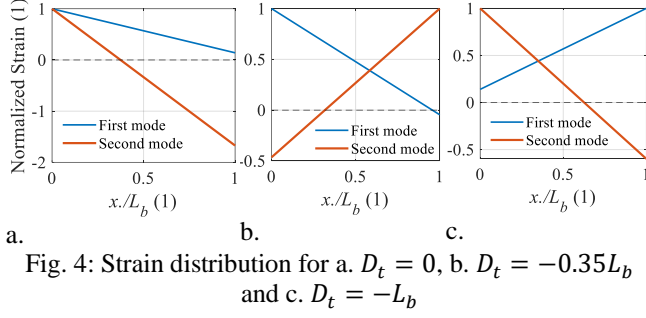
As $\phi''(x)$ is an affine function, the location where the strain is maximized correspond to the longest location of the beam where $\phi''(x)$ keeps the same sign (positive or negative). While the strain homogenization should be analyzed for an accurate electrode placement [6], the location of maximum strain should preferred for placing the piezoelectric patches. This location can be determined by finding the coordinate x, noted x_{0i}, that nullifies $\phi_i''(x)$. If $x_{0i}/L_b > 0.5$, the piezoelectric patches have to be placed close to the clamped end. If $x_{0i}/L_b < 0.5$, the piezoelectric patches have to be placed close to the tip end of the beam.

From equation (3), the value of x_{0i}/L_b is expressed as a function of a_i and b_i in equation (12).

$$\frac{x_{0i}}{L_b} = \frac{b_i + a_i}{a_i} \quad (12)$$

The next figure represents x_{0i}/L_b as function of the value of D_t/L_b for the geometrical parameters from Table 1.
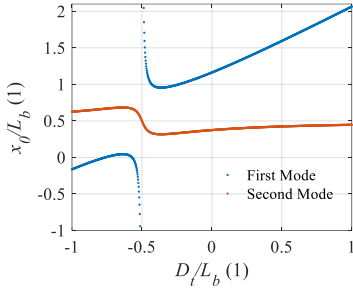
Fig. 5: Location of strain nodes x_{0i}/L_b (zero of $\phi''(x)$) as a function of the position of the proof mass gravity center

We notice that if $D_t > -0.5L_b$, x_{01}/L_b is greater than 0.5 for the first mode. The piezoelectric patches should be placed close to the clamped end. On the opposite, x_{01}/L_b is lower than 0.5 if $D_t < -0.5L_b$. In this case, the piezoelectric patches have to be placed close to the tip end.

The second mode follows the reverse rule of the first mode: x_{02}/L_b is lower than 0.5 if $D_t > -0.5L_b$ and the piezoelectric patches must be closed to tip end. the piezoelectric patches have to be close to the clamped end if $D_t < -0.5L_b$.

Finally, the strain distribution does not nullify in the beam when we have $x_{0i}/L_b > 1$ and $x_{0i}/L_b < 0$. It is interesting to notice that the above guidelines deduced from Fig. 5 are verified with the cases represented in Fig. 4. The next section concerns the experimental validation with the design of a piezoelectric cantilever with two close resonant frequencies.

IV. EXPERIMENTAL VALIDATION

A. Validation

A PZT cantilever has been designed with a L-shaped proof mass. As represented in Fig. 6.a, 4 piezoelectric are glued at each side of the beam to control the configuration of the connected electrodes. The piezoelectric patches are connected in pairs, in parallel, creating 4 distinct electrodes whose voltage is measured relative to ground and that can be connected in parallel. The parameters L_b, B, h_p and h_s of the prototype are the ones of Table 1. The proof mass is made of steel and an aluminum piece is used to raise the mass relative to the beam. Note that this aluminum piece has been neglected in the model.
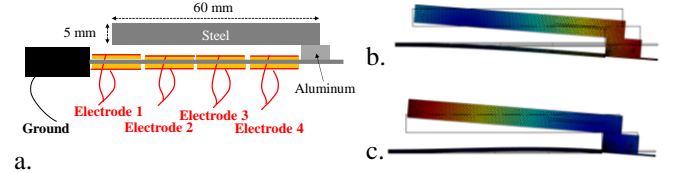
Fig. 6: a. Representation of the prototype, b. mode shape of the first mode from FEM, c. of the second mode

Fig. 6.b. and c. represents the mode shapes from 2D Comsol simulations (FEM). The normalized strain from the model is compared to FEM for the two first bending modes when the electrodes are short-circuited in Fig. 7. It reveals the good match between the proposed model and FEM.
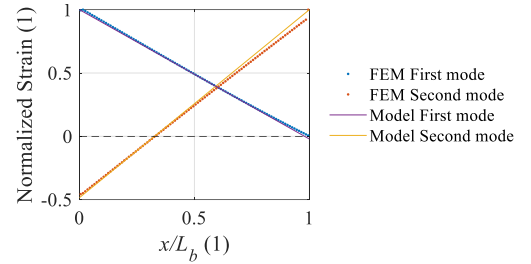
Fig. 7: Normalized strain in the proposed configuration deduced from the model and 2D Comsol simulations

Fig. 8 shows a picture of the prototype. An impedance analysis has been performed on the prototype when all the 4 electrodes connected in parallel to compare the experimental resonant frequencies and electromechanical coupling coefficients k^2 with the model and FEM simulations. Fig. 9 represents the measured admittance and the fitted model for the two first resonant frequencies of the prototype.
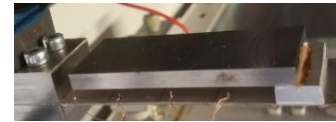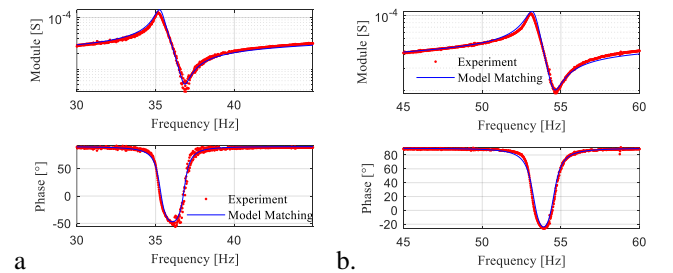
Fig. 8: Picture of the prototype

Fig. 9: Measured admittance and fitted model when all the electrodes are connected. a. First mode, b. second mode

The value of the experimental short circuit resonant frequencies and the associated k^2 are compared to the model and FEM in Table 2. This table shows that the proposed model as well as the FEM allow the accurate prediction of the frequency ratio and k^2. The difference in the resonant frequencies' values is explained by the aluminium piece (Fig. 6) that is not considered in the model, and from the spacings between the patches in FEM. Since all the electrodes are connected and the strain changes sign along the beam for the second mode compared to the first mode (Fig. 7), k^2 is lower for the second mode than for the first mode in Table 2.

Table 2: Results from the model, FEM and measurements when the 4 electrodes are connected in parallel

	Model	FEM	Measurement
First resonant frequency f_1	45.3 Hz	40.5 Hz	35.3 Hz
Second resonant frequency f_2	64.0 Hz	61.6 Hz	53.2 Hz
Frequency ratio f_2/f_1	1.42	1.52	1.51
First mode k^2	8.8 %	8.5 %	8.6 %
Second mode k^2	3.7 %	3.4 %	4.8 %

B. Discussion on electrode placement

Impedance analyses were performed on the prototype to determine k^2 when the electrodes 1 & 2 as well as electrodes 3 & 4 are connected. The values are provided in Table 3.

Table 3: Coefficient k^2 for electrodes configurations

	Electrodes 1 & 2	Electrodes 3 & 4
First mode k^2	9.4 %	0.3 %
Second mode k^2	≈ 0 %	8.1 %

Table 3 reveals the importance of the electrode configuration. As D_t is greater to $-0.5L_b$ ($D_t \approx -0.4Lb$), the electrodes close to the clamping end have to be connected for the first mode and close to the tip end for the second mode. Despite the absence of strain nodes at the first mode, k^2 is greater with the connection of electrodes 1 & 2 than of all the electrodes. This is due to the better homogeneity of the strain at the location where the electrodes are connected for the electrodes 1 & 2 configuration [6]. For the second mode, k^2 is multiplied by almost 1.7 when going from the all electrodes configuration to the electrodes 3 & 4 configuration.

The extracted mean power on resistive loads ($P = V_{rm}^2/R_{load}$) was measured under a sinusoidal excitation at 0.1 m/s² amplitude with 20 resistances and 48 frequencies. Fig. 10 depicts the maximum extracted powers obtained at optimal resistive loads. For this level of vibration amplitude, the mechanical quality factor Q_m of the prototype is estimated at about 40. As $k_e^2Q_m$ is greater than 2 for the two modes when all the electrodes are connected, the maximal theoretical power from the harvester is reached at the resonance for the optimal resistances (Fig. 10) [5].
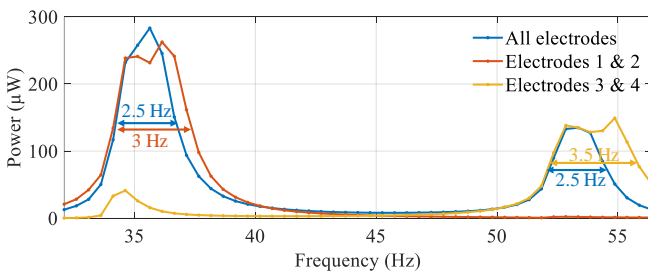

Fig. 10: Extracted power for optimal resistive loads. The frequency bandwidths are given at half of maximal power.

Therefore, increasing the coupling coefficient by mean of electrodes configuration does not lead to an increase of power. As explained in [7], the power is slightly higher around the first mode when all the electrodes are connected than when only 1 & 2 are connected. This is due to the interaction between the two bending modes, called bimodal resonance in [7], when all the electrodes are connected. Nevertheless, thanks to the increase of k^2 and the resistive electrical tuning, the frequency bandwidth increases when the electrodes 1 & 2 are connected, for the first mode (from 2.5 Hz to 3 Hz) and when the electrodes 3 & 4 are connected, for the second mode (from 2.5 Hz to 3.5 Hz). Finally, we developed a harvester with two close resonant frequencies and having a broadband behaviour on each mode by connecting the right electrodes.

CONCLUSION

As the electrode configuration is critical for the design of piezoelectric cantilever with proof mass, we propose an analytical model to analyze their strain distribution, including ones with L-shaped proof mass. The latter allows to bring closer the resonant frequencies of the two first bending modes. The model is validated by FEM an experiment. The fabricated prototype exhibits resonant frequencies of 35.3 Hz and 53.2 Hz (ratio of 1.51) and the coupling coefficient k^2 is up to 9.3 % for the first mode and to 8.1 % for the second mode. These couplings allow to reach frequency bandwidths of 3 Hz (8.4 %) and 3.5 Hz (6.5 %) respectively. Future works involve the modelling of the electrode configuration for accurate prediction of their placement and the design of an electrical interface able to dynamically select the electrodes.

REFERENCES

[1] K. Moon, J. Choe, H. Kim, D. Ahn, et J. Jeong, « A method of broadening the bandwidth by tuning the proof mass in a piezoelectric energy harvesting cantilever », *Sens. Actuators Phys.*, vol. 276, p. 17-25, juin 2018, doi: 10.1016/j.sna.2018.04.004.

[2] A. Erturk, J. M. Renno, et D. J. Inman, « Modeling of Piezoelectric Energy Harvesting from an L-shaped Beam-mass Structure with an Application to UAVs », *J. Intell. Mater. Syst. Struct.*, vol. 20, nº 5, Art. nº 5, mars 2009, doi: 10.1177/1045389X08098096.

[3] W. G. Li, S. He, et S. Yu, « Improving Power Density of a Cantilever Piezoelectric Power Harvester Through a Curved L-Shaped Proof Mass », *IEEE Trans. Ind. Electron.*, vol. 57, nº 3, p. 868-876, mars 2010, doi: 10.1109/TIE.2009.2030761.

[4] A. Erturk, P. A. Tarazaga, J. R. Farmer, et D. J. Inman, « Effect of Strain Nodes and Electrode Configuration on Piezoelectric Energy Harvesting From Cantilevered Beams », *J. Vib. Acoust.*, vol. 131, nº 1, Art. nº 1, 2009, doi: 10.1115/1.2981094.

[5] D. Gibus *et al.*, « Strongly coupled piezoelectric cantilevers for broadband vibration energy harvesting », *Appl. Energy*, vol. 277, p. 115518, nov. 2020, doi: 10.1016/j.apenergy.2020.115518.

[6] K. Hu, B. Zhou, F. Wang, Z. Yang, et M. Wang, « Influence of effective electrode coverage on the energy harvesting performance of piezoelectric cantilevers », *Energy Convers. Manag.*, vol. 248, p. 114758, nov. 2021, doi: 10.1016/j.enconman.2021.114758.

[7] A. Morel, D. Gibus, et A. Badel, Adrien, « Exploring the power-limit of multi-modes multielectrodes vibration energy harvesters », présenté à IEEE Wireless Power Week, Bordeaux, 2022.